Residual Stress-Driven Non-Euclidean Morphing in Origami Structures

Zihe Liang[1†], Sibo Chai[2,3†], Qinyun Ding[1], Kai Xiao[1], Ke Liu[4], Jiayao Ma[2,3*], Jaehyung Ju[1*/]

[1]UM-SJTU Joint Institute, Shanghai Jiao Tong University, 800 Dongchuan Road, Shanghai 200240, China

[2]Key Laboratory of Mechanism and Equipment Design of Ministry of Education, Tianjin University, Tianjin 300350, China

[3]School of Mechanical Engineering, Tianjin University, Tianjin 300350, China

[4]Department of Advanced Manufacturing and Robotics, College of Engineering, Peking University, Beijing 100871, China

Abstract:

Non-Euclidean surfaces are ubiquitous in numerous engineering fields, such as automotive, aerospace, and biomedical engineering domains. Morphing origami has numerous potential engineering applications, including soft robots, mechanical metamaterials, antennas, aerospace structures, and biomedical devices, owing to its intrinsic morphing features from two-dimensional (2D) planes to three-dimensional (3D) surfaces. However, the current one-dimensional (1D) hinge deformation-driven transformation of foldable origami with rigid or slightly deformable panels cannot achieve a 3D complex and large curvilinear morphing. Moreover, most active origami structures use thin hinges with soft materials on their creases, thus resulting in a lower load capability. This study proposes a novel origami morphing method that demonstrates large free-form surface morphing, e.g., Euclidean to non-Euclidean surface morphing with shape-locking. We embedded tensorial anisotropic stress in origami panels during the extrusion-based 3D printing of shape memory polymers. The extrusion-based 3D printing of isotropic shape memory polymers can produce tensorial anisotropic stress in origami panels during fabrication, which can realize large non-Euclidean surface morphing with multiple deformation modes. The connecting topology of the origami unit cells influences the global morphing behavior owing to the interaction of the deformation of adjacent panels. Non-Euclidean morphing integrated with four-dimensional (4D) printing can provide multimodal shape locking at material and structural levels. The non-Euclidean surface morphing caused by tensorial residual stress in the panel during 3D printing expands the design space of origami and kirigami structures.

Keywords – origami, panel deformation, 4D printing, instability, shape memory effect, morphing

---

[1] †   These authors contributed equally to this work.

*   Corresponding authors: jiayao.ma@tju.edu.cn (J. M.); jaehyung.ju@sjtu.edu.cn (J. J.)

I. Introduction

Morphing shapes from a two-dimensional (2D) plane to a three-dimensional (3D) space can significantly influence future manufacturing, such as in Industry 4.0, which requires customized mass production and convenient logistics for storage and transportation[1,2]. Moreover, morphing complex geometries from a 2D plane to a 3D curved non-Euclidean surface can reduce manufacturing costs by directly embedding the design into the manufacturing process. The morphing involved in manufacturing does not require additional labor to assemble 3D shapes owing to the single-step fabrication followed by morphing[3–5]. Morphing does not require the use of supporting materials for the 3D printing of overhang features. This reduces fabrication energy requirements by increasing the manufacturing speed owing to the reduction of fabrication volume without use of supporting materials[6,7]. The physical properties and functionality of the morphed shapes can be tuned as a byproduct. The morphing strategy can be more useful in micro- and nano-fabrication, where the direct fabrication of 3D complex geometries is challenging. However, 2D plane-based fabrication is more conventional, e.g., electron beam nanolithography[8–10] and atomic layer deposition[11,12].

Owing to the intrinsic features of the origami (or kirigami), folding of a 2D plane shape into a 3D free-formed one, morphing is especially beneficial for fabricating origami structures. The high-level foldability of origami structures enables the production of self-foldable structures and active metamaterials. However, current origami structures have a limitation of morphing into non-Euclidean surfaces that are ubiquitous in the automotive, aerospace, and ocean engineering fields[13]. Despite the existing applications of origami in robotics[14,15], deployable structures[16,17], and biomedical devices[18,19], the transformed configurations of origami structures have retained flat plates, thus globally generating a discretized geometry due to the use of simple one-dimensional (1D) deformation mechanisms on the hinges such as bending/folding[20,21] or twisting[22].

Four-dimensional (4D) printing is a common method for demonstrating the morphing of simple origami structures by integrating functional materials and additive manufacturing[21,23]. Embedding entropy, e.g., internal stress, in the 3D printing of smart materials, is a typical strategy in 4D printing[24–26]. However, most 4D printing techniques are limited with respect to the synthesis of strong, morphable, and 3D curvilinear structures. Most membrane-based 4D printing methods with a heterogeneous distribution of scalar entities with physical or chemical potential[27,28] cannot be scaled up to structural applications owing to the extremely low stiffness of the base materials ($E < {\sim}0.5 MPa$) and thin membrane dimension[23,27,29]. Without embedding spatial anisotropy with reinforcement and shape locking during fabrication, 3D curvilinear structures cannot be realized using scalar field gradient-based 4D printing[27,28,30,31].

To address the dual challenges of active origami and 4D printing, reforming the conventional transformation strategy of origami from hinges to panels is necessary; this can be achieved by programming using high-level physical intelligence during additive manufacturing. In this study, tensorial anisotropic residual stress was embedded into a thick panel during the 3D printing of a shape memory polymer to morph a flat surface into those with nonzero Gaussian curvatures, while exhibiting dual shape-locking modes at the material and structural levels. This work demonstrates that tensorial anisotropic stress embedded in a flat plate[31–33] during 3D printing can generate 3D curvilinear self-foldable origami structures with multiple deformation modes and connection effects.

II. 4D printing of non-Euclidean surfaces

Most reconfigurable structures, including origami, use hinge deformation with simple folding/bending modes[20,21,34] to create discrete and noncurvilinear geometries. The hinge deformation-driven self-folding origami harnesses a vector field controlled by the temperature or moisture gradient. Unlike the hinge-driven folding shown in Figure 1a, embedding a tensor field into panels can produce complex morphing shapes while transforming the flat panels into a non-Euclidean surface, as demonstrated by the manufacture of the Yoshimura origami patterns shown in Figure 1a.

Non-Euclidean morphing can be implemented using extrusion-based 3D printing such as direct ink writing (DIW)[35–37] or fused deposition modeling (FDM)[23,24]. Figure 1b illustrates the principle of morphing non-Euclidean surfaces by the extrusion of a single material. The extruded filaments of shape memory polymers (SMPs) are pre-stressed in the longitudinal direction with Poisson's effect in the lateral direction during the printing process above the melting temperature. This is analogous to the typical mechanical training of SMPs above their glass transition temperature (T_g). The printed flat panel retains its tensorial internal stress and is fixed at room temperature. Reheating above the T_g of the SMP causes the filaments to deform, thus transforming them to a low-energy state by releasing energy while exhibiting a shape-memory effect. Combining this principle with multilayer printing in different printing directions can introduce more complex tensorial residual stress during printing, thus producing a morphed structure with complex surface shapes, such as doubly curved surfaces with negative Gaussian curvatures. Notably, the pre-stressed filaments layered with $\left[\theta_{top}, \theta_{botton}\right] = [45°, -45°]$ produce a saddle-shaped surface, as illustrated in Figure 1c. Moreover, the morphed structure exhibits two shape-locking modes. The first is the locking mode of the material with the shape-fixity effect of the SMP when the temperature decreases after the initial thermal deployment above T_g. The second is structural locking due to mechanical instability, which is discussed in Section V. After the initial thermal deployment, the shape of the bistable curved tube changes to a different low-energy state through mechanical loading, as shown in Figure 1d. The bistable structure produces two different lockable modes that are longitudinally and laterally transformed by the connection topology of the panels.
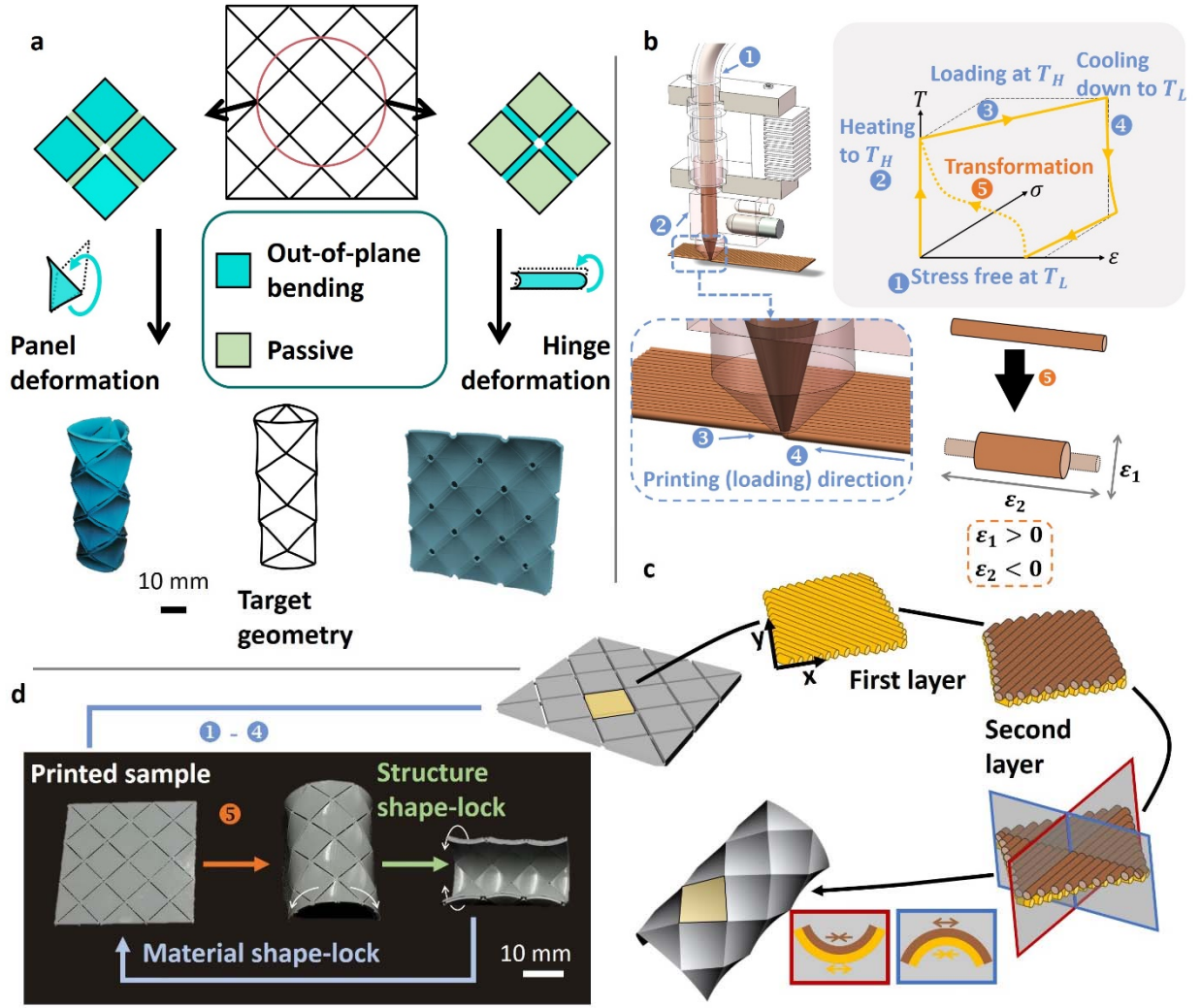
*Figure 1. **Panel deformation-based self-foldable origami manufacturing**, a. Comparison of two origami manufacturing methods for the fabrication of a Yoshimura pattern: the conventional soft hinge-driven transformation has a limitation in transforming complex structures. Moreover, the panel deformation can produce more complex transformations such as a non-Euclidean surface and large deformation. **b.** 4D printing of a single material to produce anisotropy and the shape memory effect. **c.** Programming with tensorial stress on the panel to morph into a non-Euclidean structure, e.g., a Yoshimura pattern, with doubly curved surfaces, **d.** Experimental demonstration of self-foldable origami structures with multimodal shape locking.*

III. Thermomechanical modeling of panel deformation

To demonstrate panel deformation programming using direct 4D printing, we developed a theoretical model for the thermomechanical shape morphing of a flat panel. Subsequently, we implemented a mathematical relationship to describe the connectivity between the individual and adjacent plates during shape morphing.

We adopted the classical laminated plate theory (**CLPT**), where we obtained the in-plane strain ($\boldsymbol{\varepsilon^0}$) and out-of-plane curvature ($\boldsymbol{\kappa}$) by computing the effect of the external resultant loadings, force (**N**), moment (**M**), thermal resultant loadings, thermal force ($\mathbf{N^T}$), and thermal moment ($\mathbf{M^T}$) on the printed bilayer laminated composites. The material properties and layer (or ply) orientations of the bilayer composite contribute to $\mathbf{A}, \mathbf{B},$ and $\mathbf{D}$, which represent the extensional, bending-extensional, and

bending stiffness tensors, respectively. The superscript '0' of the strain indicates the midplane of the plate. The thermomechanical constitutive relationship is expressed as follows[38]:

$$\begin{Bmatrix} \mathbf{N} \\ \mathbf{M} \end{Bmatrix} = \begin{bmatrix} \mathbf{A} & \mathbf{B} \\ \mathbf{B} & \mathbf{D} \end{bmatrix} \begin{Bmatrix} \boldsymbol{\varepsilon}^{\mathbf{0}} \\ \boldsymbol{\kappa} \end{Bmatrix} - \begin{Bmatrix} \mathbf{N^{T}} \\ \mathbf{M^{T}} \end{Bmatrix}. \tag{1}$$

Notably, the three stiffness tensors ($\mathbf{A}$, $\mathbf{B}$, and $\mathbf{D}$) are determined by the anisotropic material modulus and Poisson's ratio of the SMP material, in addition to the printing pattern of each layer. The resultant thermal loadings are determined from the longitudinal shrinking strain of the SMP fibers when considering Poisson's effect. We adopted polylactic acid (**PLA**) as an SMP material, with its longitudinal shrinkage values dependent on the exposed time and actuation temperature; as adopted from prior research[24,39,40] for a nozzle speed of $60\ mm/s$, nozzle temperature of $210\ °C$, and layer height of $0.1\ mm$. The expressions for each term are expressed by Equation (S9) in Section S1 of the Supplementary Information (SI), and the material properties in Section S3 of the SI.

The Green–Lagrange strain tensor $\boldsymbol{\varepsilon}\left(= \boldsymbol{\varepsilon}^{\mathbf{0}} + z\boldsymbol{\kappa}\right)$ is a combined function of $\boldsymbol{\varepsilon}^{\mathbf{0}}$ and $\boldsymbol{\kappa}$, where z is the distance from the midplane of the composite in the thickness direction. The components of the displacement vector $\mathbf{u}$ can be expressed as $u_i = u_i{}^0 - z\frac{\partial u_3{}^0}{\partial X_i}$ for $i = 1,2$ and $u_3 = u_3{}^0$, where X_i is the basis vector components and $u_i{}^0$ is the midplane displacements. From the strain–displacement relationship, we can obtain $\mathbf{u}$ to predict the deformed configurations of a single plate:

$$\boldsymbol{\varepsilon} = \frac{1}{2}[(\boldsymbol{\nabla}_{\mathrm{x}}\mathbf{u})^T + \boldsymbol{\nabla}_{\mathrm{x}}\mathbf{u} + (\boldsymbol{\nabla}_{\mathrm{x}}\mathbf{u})^T\boldsymbol{\nabla}_{\mathrm{x}}\mathbf{u}]. \tag{2}$$

To solve Equation (2), we imposed boundary conditions $\mathbf{u} = const$ on Γ_u, where Γ_u is the surface boundary. The explicit expression of the boundary condition of the laminated segments varies with the printing direction of the layer, and the boundary condition of the laminates is presented in Section S1 of the SI. Figure 2a illustrates the thermomechanical shape morphing of a single $[45°, -45°]$ laminated rhombus plate, which was initially flat and then deformed to a doubly curved surface in a non-Euclidean space. In particular, a, b, and d denote the geometric parameters in the undeformed configuration; and $\bar{a}$ is the length of a deformed plate, whereas $\bar{b}$ and $\bar{d}$ are the diagonal lengths along the lateral and longitudinal directions, respectively.

IV. Connecting topology effect on morphing

Assembly with connection of vertices

Considering the continuity of individual segments, the global deformation of the assembled panels can be estimated when the deformed configurations of the panel are known. For example, a rhombus panel with a negative Gaussian curvature can be 4D printed, as shown in Figure 2a. The in-plane tessellation of a $[45°, -45°]$ laminated panel with a connection at the vertices can generate a cylindrical shape such as a Yoshimura pattern[41] with a global zero-Gaussian curvature, as shown in Figure 2b. The deformed configuration of an assembly of rhombus panels can be expressed as follows:

$$\tan\frac{\varphi}{4} = \frac{\sqrt{4\bar{a}^2 - \bar{b}^2 - \bar{d}^2}}{\bar{b}}. \tag{3}$$

Notably, φ characterizes the circumferential deformation of a single rhombus panel. The deformation magnitude of the assembly can be expressed as a global curvature κ_g, which is defined as $\kappa_g = 1/r_g$, where r_g denotes the radius of the global curvature generated by the interaction of individual panels and hinges. Equation (3) reveals that the global curvature is a function of the rhombus angle α. The explicit definition of r_g is expressed in Section S1 of SI.

Figure 2c presents the geometric parameters of the assembly, including the hinge length l_c, hinge width d_c, panel thickness t_p, and hinge thickness t_c. The deformed shape in Figure 2b was generated with $t_p = 2\,mm$, $t_c = 0.4\,mm$, $l_c/d = 0.2$, and $d_c/d = 0.05$ for $d = 16\,mm$. The local deformation of the individual panels interacted with the hinges to form a globally deformed shape. Figure 2e presents the deformation of the hinges along the circumferential direction of the cylinder when the panels were connected at the vertices. Notably, a panel with $\alpha = 90°$ produces a doubly curved surface with two principal directions: circumferential and longitudinal. Global deformation occurred along the circumferential direction, which requires less energy than longitudinal deformation. The hinges generated a convex shape along the circumferential direction to align with the convex principal curvature of the panels, as shown in Figure 2e. However, the thermomechanical strain energy did not overcome the energy barrier in the longitudinal direction, where the concave principal curvature shape of the panel did not influence the global shape. Moreover, only the hinges deformed to match the continuity of Elastica[42].

The thickness ratio $R_{lt}(= t_1/t_p)$ of the panel layups can influence the local curvature κ of panels and κ_g. Figure 2f presents κ_g values of assemblies with $\alpha = 90°$ for varying R_{lt} values, presenting a comparison of the values for analytical models in Section S1 of the SI, finite element (FE) simulations, and experiments with 3D scanned data. Figure 2g presents a design map of κ_g for varying α and R_{lt} values. Notably, the assembly with $R_{lt} = 0.5$ and $\alpha = 90°$ exhibited a

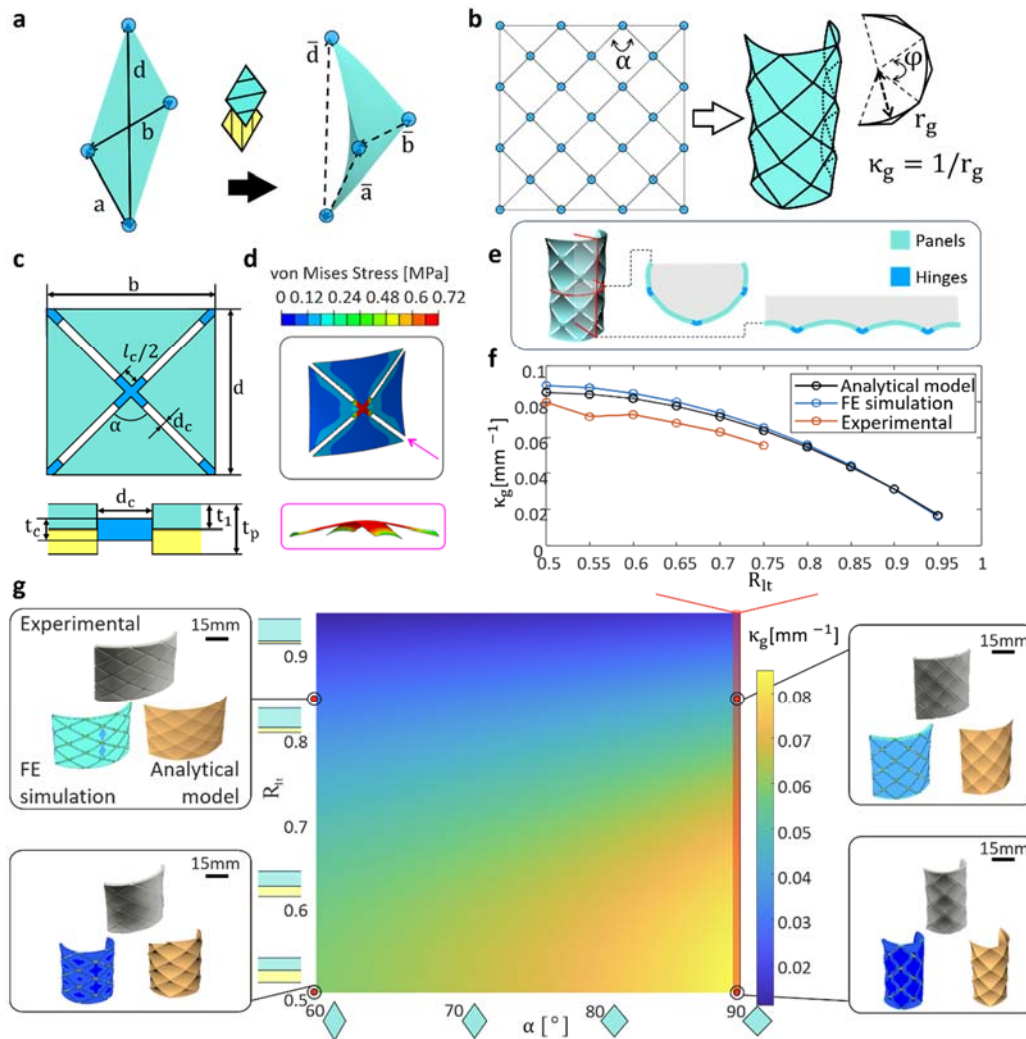bistable property, as shown in Figure 1d and Supplementary Video S3; this is further discussed in Section V.

Figure 2. **Thermomechanical deformation of a vertex-connected pattern. a.** Deformation of a single rhombus unit. **b.** Deformation of a 3 × 3 vertex-connected pattern. **c.** Geometric parameters of the vertex-connected pattern. **d.** Local crease deformation of the vertex-connected pattern with parameters ($\alpha = 90°$ and $R_{lt} = 0.5$). **e.** Deformed configuration of a 3 × 3 vertex-connected pattern with crease design, and its cross-section profiles **f.** Comparison of the global curvature κ_g for varying thickness ratios R_{lt} in the analytical model, FE simulation, and experiment. **g.** Design map for κ_g obtained by the analytical model for varying α and R_{lt} values.

Assembly with edge connection

In addition to the connection of the vertices, we investigated the topology effect of an assembly on the global deformation by changing the link location from the vertices to the mid-edges, as shown in Figure 3a. Figure 3b presents a comparison of the κ_g values of assemblies with 3 × 3 units for the vertex-connected and mid-edge connected conditions with respect to varying R_{lt} and α values, which indicates that a mid-edge connection produces a lower κ_g due to the hinge alignment along

the off-principal curvature directions of deformed panels. The mid-edge hinges have a torsional deformation mode to satisfy the continuity of the adjacent deformation of panels along the off-diagonal curvature directions, and Figure 3c presents evidence of a lower κ_g in Figure 3b.

Similar to the vertices connection, the assembly with $R_{lt} = 0.5$ and $\alpha = 90°$ in the mid-edge connection exhibited a bistable property by the competition of deformation between the longitudinal and circumferential directions with instability. Figure 3d presents a further parametric study of κ_g with respect to two varying geometric parameters: the hinge length l_c and hinge thickness t_c (or $\alpha = 90°$ and $R_{lt} = 0.5$). In particular, a greater l_c and smaller t_c produced a high κ_g, which is related to simple torsional deformation in the hinges.
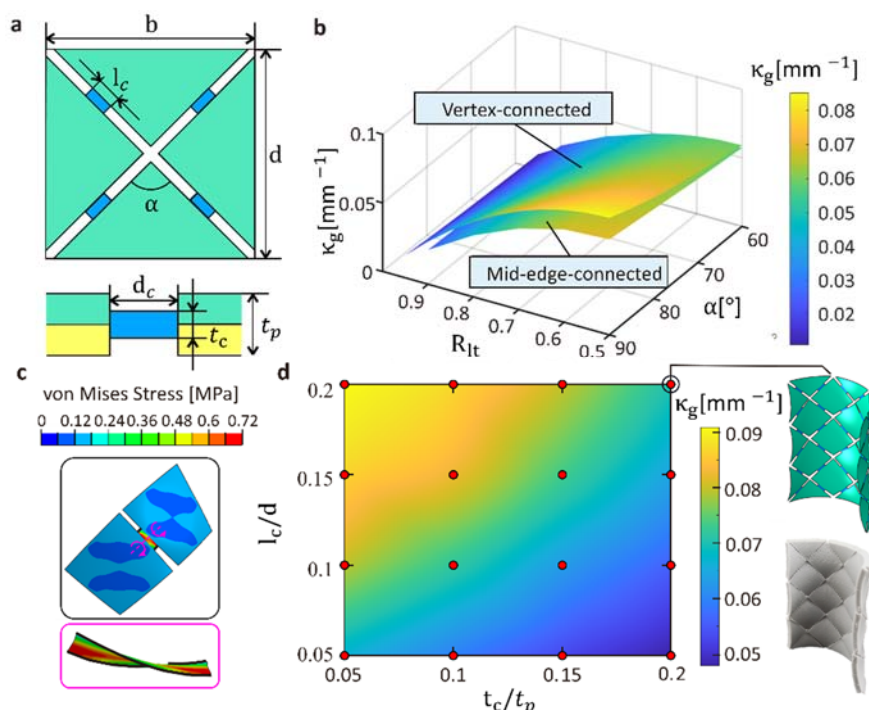

Figure 3. **Thermomechanical deformation of an edge-connected pattern; a.** Geometric parameters of the edge-connected pattern. **b.** Comparison of global curvature for the vertex-connected and the mid-edge-connected patterns for varying α and R_{lt} values. **c.** Local crease deformation of the structure with parameters of $\alpha = 90°, R_{lt} = 0.5, t_c/t_p = 0.2,$ and $l_c/d = 0.2$. **d.** Relationship between the normalized crease thickness and crease length with respect to the global bending of the 3 × 3 units, in addition to the deformed configuration and local crease deformation of the structure with parameters of $t_c/t_p = 0.2$ and $l_c/d = 0.2$.

V. Bistability of 4D printed origami

A rhombus unit with $R_{lt} = 0.5$ and $\alpha = 90°$, as shown in Figure 2a, thermally morphed into a surface with negative Gaussian curvature. The FE simulations and experiments demonstrated no snapping bistability of the saddle geometry transformed from the rhombus unit, as presented in Section S4 of the SI and Supplementary Video S8. However, when the rhombus unit was connected to adjacent units and thermally transformed, it was bistable. Figure 4a presents a phase map of the bistability of an extended unit comprising four halves of rhombus panels connected to the vertices at

the center and four corners. For varying α and R_{lt} values, the phase map obtained from FE simulations exhibited three distinctive regions: bistable, monostable, and no negative stiffness. A greater α and smaller R_{lt} provide a higher probability of the bistability of the extended unit. Figure 4b presents the vertical force–deflection curves of the extended units after thermal transformation. We obtained a reaction displacement for a vertical force at the top center, whereas the four corner nodes were allowed to slide in the plane direction. Figure 4b presents three representative force–deflection behaviors, i.e., bistable $(B_2/B_1 < 0)$, monostable $(0 \le B_2/B_1 \le 1)$, and monotonic $(B_2/B_1 > 1)$; where B_1 and B_2 are the local maximum and minimum loads, respectively. See Supplementary Video S2 for the deformation animation.
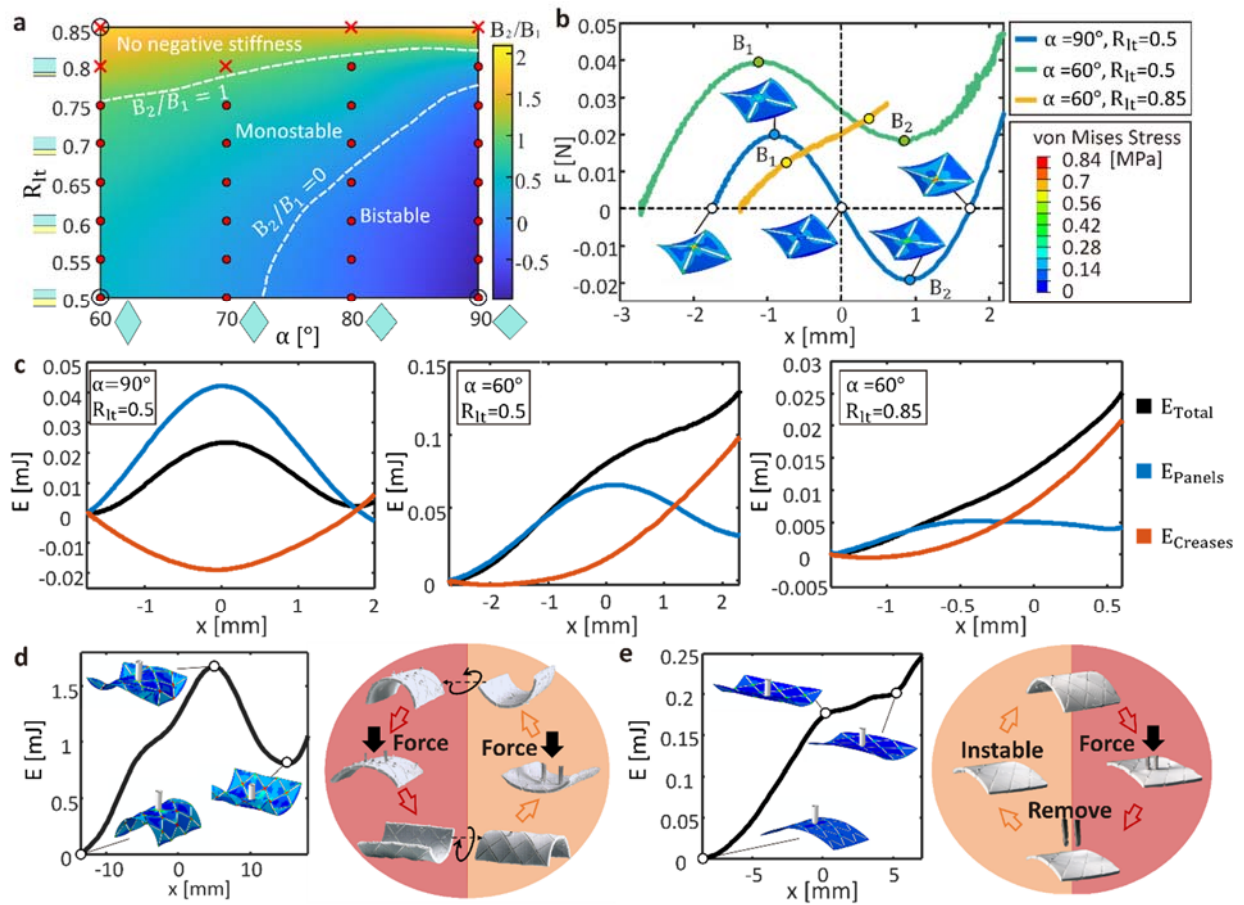

Figure 4. **Bistability of the vertex-connected pattern. a.** Design map of bistability obtained from FE simulations for varying α and R_{lt} values. **b.** Representative force–displacement curves of bistable, monostable, and monotonic states. **c.** Energy composition: total energy, energy by panel deformation, and energy by crease deformation in three representative units. **d.** Force–displacement curve of a bistable 3 × 3 vertex-connected assembly (α = 90° and R_{lt} = 0.5) and its experimental validation. **e.** Force–displacement curve of a monostable 3 × 3 vertex-connected pattern (α = 60° and R_{lt} = 0.85) and its experimental validation.

By decomposing the total energy into those of panels and creases during the snapping process, we found that the total strain energy was in accordance with the crease energy pattern instead of the panel energy pattern, as shown in Figure 4c, which confirms that the connection effect of the rhombus units significantly influences bistability. Figure 4d illustrates the bistable snapping phenomenon of the 3 × 3 assembly with $\alpha = 90°$ and $R_{lt} = 0.5$, whereas Figure 4e demonstrates the monostable

snapping for $\alpha = 60°$ and $R_{lt} = 0.85$ (Supplementary Video S3). The bistable and monostable behaviors of the assemblies were in accordance with those of the extended unit cells.

VI. Multimodal geometric morphing and stiffness

Panel-deformation-driven origami can be extended to multimodal deformations. Figure 5a–5d demonstrate the direct 4D printing of a human mask and the wrapping pattern conceptualized by the thermomechanical composite laminate model integrated with the anisotropically extruded SMP. By encoding five and three deformation modes for the human mask and wrapping pattern, respectively, the printed 2D plates were morphed into 3D complex shapes with individual curvatures after exposure to high temperatures, as shown in Figure 5b and 5d. Notably, the large and multimodal deformations of individual panels were independently controlled, whereas the connection at the vertices adjusted the global shapes.
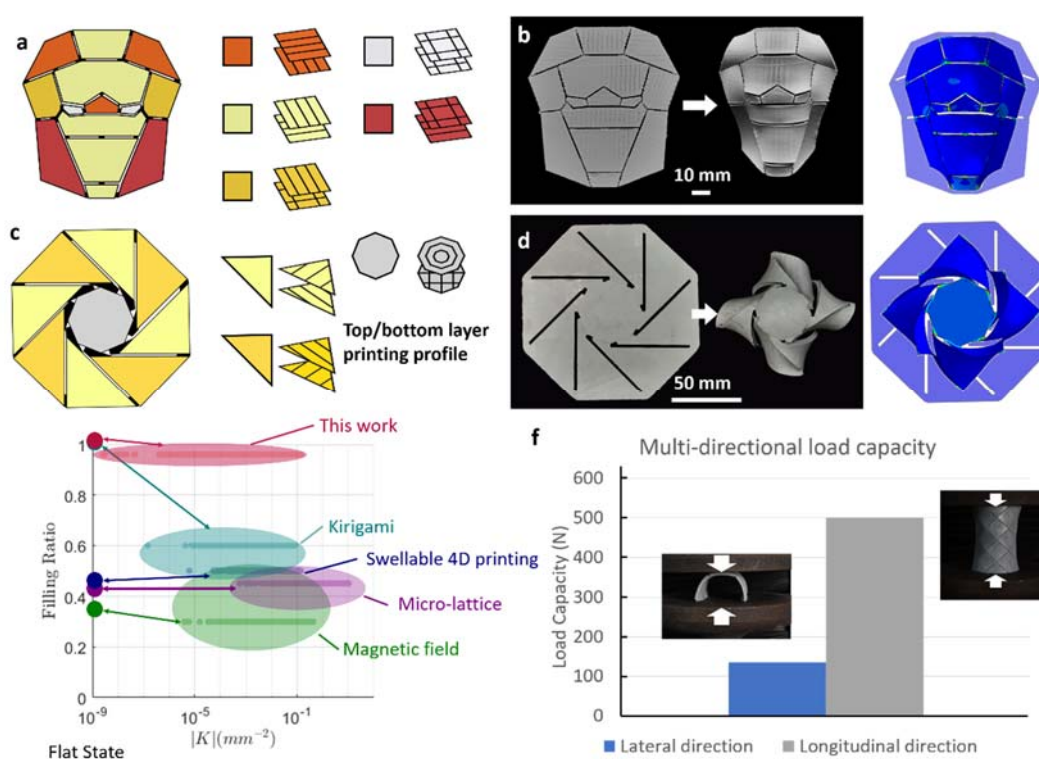

Figure 5. **Complex panel-deformation-driven morphing with multimodal deformation and high stiffness; a.** *Design of a human mask with panels that are individually encoded with different laminate layups.* **b.** *Experiment and FE simulation of the thermomechanical deformation of the human mask* **c.** *Design of a wrapping pattern with panels that are individually encoded with different laminate layups.* **d.** *Experiment and FE simulation of the thermomechanical deformation of a wrapping pattern.* **e.** *Comparison of the Gaussian curvature ranges for the filling ratios of varying structures with a Kirigami tessellation approach[43], hydrogel 4D printing approach[23], micro-lattice design[3], and Lorentz force-based metasurface[44], where the solid circles on the vertical axis denote the initial flat state.* **f.** *Load carrying capacity of panel-deformation-driven origami structures in the lateral and longitudinal directions.*

Implementing large deformations with high stiffness is practically challenging. Low-stiffness materials such as elastomers and hydrogels[27,30] or structures with high porosity, such as kirigami and lattice materials[3,23,43,44], can be used to readily implement large deformations; however, they are weak for

structural applications. The panel-deformation-driven morphing, in addition to the shape fixity of the SMP in this study, can increase the filling ratio for high stiffness while exhibiting shape-morphing capacity for complex 3D curvilinear surfaces, as shown in Figure 5e (See Section S8 of SI for details). Kirigami structures are highly compact before morphing, and lose their filling ratios after morphing[43]. However, the origami with panel-deformation-driven morphing did not undergo a significant change in filling ratio after morphing, thus maintaining its structural potential after morphing, as shown in Figure 5e. Figure 5f demonstrates the high load capacity of a Yoshimura patterned structure ($R_{lt} = 0.5$, $\alpha = 90°$) in the longitudinal and lateral directions. Compared with the loading capacity of other structures[3,45], the proposed structure exhibited a higher capacity than the origami and kirigami structures by a factor of approximately 10. See Section S8 of the SI for more details on mechanical testing.

VII. Discussion

To realize the non-Euclidean surface deployment of the origami structures with large deformation and high stiffness, the proposed method overcomes conventional hinge-based origami folding[21,34,46]. The anisotropic stress field embedded with the shape memory effect of polymers into panels during extrusion-based additive manufacturing can produce a 3D curvilinear deployment of origami structures with varying Gaussian curvatures. The unique method proposed in this study can realize multimodal shape locking at the material and structural levels, which can contribute to numerous potential applications of active origami structures with relatively high stiffnesses, such as robotic metamaterials[46,47], antennas[26], solar arrays[16], morphable automotive structures[27], and biomedical devices[19,48].

Most studies on shape morphing from the 2D plane to 3D space have been conducted with cellular structures[3,26,43] or soft materials[23,27] to realize a larger morphing capacity. These materials cannot be used for scaled-up structural applications owing to their minimal load-carrying capacity. Moreover, although the high foldability of origami (or kirigami) provides a solution for the structural design of 2D–3D shape morphing, current highly discretized origami with flat panels cannot match the morphing capabilities of cellular structures. Notably, the proposed thick panel-deformation-driven active origami can be used to design thick panels with stiffer materials, which contribute to a higher global stiffness of structures while providing a relatively wide range of shape morphing (Figures 5e and 5f). The SMP shape memory and shape fixity effects can facilitate the extensive structural transformation and load-carrying capabilities of origami structures, where there are differences of three orders of magnitude between the transformation and load-carrying modes.

Conventional origami structures with negative Gaussian curvatures are bistable because the traditional folding method requires the instability of the doubly curved geometry from a flat plane[49]. Notably, the panel-deformation-driven active origami structures produce instability-free Gaussian curvatures because the panel deformation mode by 4D printing is bending and not snapping, as shown in Supplementary Video S8. However, the interactions of adjacent instability-free Gaussian curvatures with the hinge topology can produce bistable structures, as shown in Figure 4.

Although the proposed active origami structures can produce large deformations of thick panels with various Gaussian curvatures, the current thin-panel-based model expressed by Equation (1) may be rendered inaccurate for the prediction of the curvature with an increase in the panel thickness. In this

study, an inverse design method was not provided for the deformation of an assembly of panels, which will be investigated in future research.

VIII. Conclusion

In summary, this study introduced a non-Euclidean morphing method of origami, which is integrated with an extrusion-based 4D printing of shape memory polymers, to demonstrate the self-deployment of origami with 3D curvilinear shapes. The programming of tensorial anisotropic residual stress into panels from isotropic shape-memory polymers during extrusion-based additive manufacturing using the thermomechanics of printed laminates can realize non-Euclidean morphing with different deformation modes, including a doubly curved surface. Combining the unique shape fixity of SMP with mechanical bistability can produce multimodal shape locking at the material and structural levels. Potential applications include deployable and tunable automobile, aerospace, and ocean engineering structures designed to reduce fluid friction on smooth surfaces. The proposed approach represents reversible, shape-lockable, and scalable morphing structures, for which conventional reconfigurable structures are yet to be developed.

IX. Materials and Methods

Sample fabrication and deployment: This work uses a Fused Deposition Modeling (FDM) 3D printer (Ultimaker 2+, Ultimaker, The Netherlands) with a commercially available polylactic acid (PLA) filament (PolyLite PLA, Polymaker) to print flat origami samples. We construct 3D models of the origami samples with a 3D CAD design software (Solidworks 2021, Dassault Systèmes), incorporating geometric parameters of origami structures such as the thickness ratio, rhombus angle, and unit connection conditions. We import 3D models into a preprocessing code of our FDM 3D printer (Ultimaker Cura 5.0.0, Ultimaker, The Netherlands), where they are sliced into G-Code files that direct the 3D printing process. We adjust the printing angles in Cura's 'Infill' section to achieve the bilayer fabrication of origami panels. Other essential printing parameters include the nozzle temperature (180 ℃), printing-layer height (0.1 mm), and print speed (50 mm/s). After printing, we deploy the samples in a hot water tank where an immersion heater (Anova, USA) maintains and monitors the temperature. The morphed origami structures made of PLA above its glass transition temperature ($T_g \geq 60℃$) lock their shapes when the temperature cools down to room temperature ($T_r \sim 20℃$).

Measurement of panel deformation: We validate the analytical and numerical models with experiments. A 3D scan system (Einscan Pro, Shining 3D) collects mesh data of the morphed origami structures. We write a MATLAB code to automatically collect individual panels' center positions from the scanned point cloud data, obtaining the global curvature of morphed origami structures.

Numerical simulations: Using ABAQUS Standard/CAE 6.14, we simulate the self-folding actuation by heating. We also use a quasi-static simulation of bistable properties of origami assemblies in Section 4 using the explicit module of ABAQUS. All parts are meshed with an S4R element in ABAQUS. See Supplementary Information for detailed simulation settings.

Acknowledgments

Author contributions

J. J. and J. M. designed the research; Z. L. and S. C. designed the structures, performed the experiments, conducted the FE simulations, and analyzed the data; Z. L. designed the 4D printing technique and developed the theoretical model; Z. L., Q. D., and K. X. collected and processed the experimental data; K. L., S. C., and Z. L. analyzed the bistability qualitatively and quantitatively; and J. J. and J. M. provided guidance throughout the research. All authors participated in writing and reviewing the manuscript.

References

1. Guseinov, R., McMahan, C., Pérez, J., Daraio, C. & Bickel, B. Programming temporal morphing of self-actuated shells. *Nat Commun* **11**, 237 (2020).

2. Ze, Q. *et al.* Magnetic Shape Memory Polymers with Integrated Multifunctional Shape Manipulation. *Advanced Materials* **32**, 1906657 (2020).

3. Cheng, X. *et al.* Programming 3D curved mesosurfaces using microlattice designs. *Science* **379**, 1225–1232 (2023).

4. Filipov, E. T., Tachi, T. & Paulino, G. H. Origami tubes assembled into stiff, yet reconfigurable structures and metamaterials. *Proceedings of the National Academy of Sciences* **112**, 12321–12326 (2015).

5. Ye, H. *et al.* Multimaterial 3D printed self-locking thick-panel origami metamaterials. *Nat Commun* **14**, 1607 (2023).

6. Hinton, T. J., Hudson, A., Pusch, K., Lee, A. & Feinberg, A. W. 3D Printing PDMS Elastomer in a Hydrophilic Support Bath via Freeform Reversible Embedding. *ACS Biomater. Sci. Eng.* **2**, 1781–1786 (2016).

7. Lee, H. *et al.* 3D-printed programmable tensegrity for soft robotics. *Sci. Robot.* **5**, eaay9024 (2020).

8. Ouk Kim, S. *et al.* Epitaxial self-assembly of block copolymers on lithographically defined nanopatterned substrates. *Nature* **424**, 411–414 (2003).

9. Kim, D.-H., Lee, H., Lee, Y. K., Nam, J.-M. & Levchenko, A. Biomimetic Nanopatterns as Enabling Tools for Analysis and Control of Live Cells. *Advanced Materials* **22**, 4551–4566 (2010).

10. Meng, H. & Li, G. A review of stimuli-responsive shape memory polymer composites. *Polymer* **54**, 2199–2221 (2013).

11. Liu, Q. *et al.* Micrometer-sized electrically programmable shape-memory actuators for low-power microrobotics. *Science Robotics* **6**, eabe6663 (2021).

12. Mackus, A. J. M., Dielissen, S. a. F., Mulders, J. J. L. & Kessels, W. M. M. Nanopatterning by direct-write atomic layer deposition. *Nanoscale* **4**, 4477–4480 (2012).

13. Xiao, K., Liang, Z., Zou, B., Zhou, X. & Ju, J. Inverse design of 3D reconfigurable curvilinear modular origami structures using geometric and topological reconstructions. *Nat Commun* **13**, 7474 (2022).

14. Ren, Z., Hu, W., Dong, X. & Sitti, M. Multi-functional soft-bodied jellyfish-like swimming. *Nat Commun* **10**, 2703 (2019).

15. Zhang, S., Ke, X., Jiang, Q., Ding, H. & Wu, Z. Programmable and reprocessable multifunctional elastomeric sheets for soft origami robots. *Science Robotics* **6**, eabd6107 (2021).

16. Chen, T., Bilal, O. R., Lang, R., Daraio, C. & Shea, K. Autonomous Deployment of a Solar Panel Using Elastic Origami and Distributed Shape-Memory-Polymer Actuators. *Phys. Rev. Appl.* **11**, 064069 (2019).

17. Jape, S. *et al.* Self-foldable origami reflector antenna enabled by shape memory polymer actuation. *Smart Mater. Struct.* **29**, 115011 (2020).

18. Zhao, W., Li, N., Liu, L., Leng, J. & Liu, Y. Origami derived self-assembly stents fabricated via 4D printing. *Composite Structures* **293**, 115669 (2022).

19. Ze, Q. *et al.* Soft robotic origami crawler. *Science Advances* **8**, eabm7834 (2022).

20. Yuan, C., Wang, T., Dunn, M. L. & Qi, H. J. 3D printed active origami with complicated folding patterns. *Int. J. of Precis. Eng. and Manuf.-Green Tech.* **4**, 281–289 (2017).

21. Ge, Q., Dunn, C. K., Qi, H. J. & Dunn, M. L. Active origami by 4D printing. *Smart Mater. Struct.* **23**, 094007 (2014).

22. Peraza-Hernandez, E. A., Hartl, D. J., Jr, R. J. M. & Lagoudas, D. C. Origami-inspired active structures: a synthesis and review. *Smart Mater. Struct.* **23**, 094001 (2014).

23. Sydney Gladman, A., Matsumoto, E. A., Nuzzo, R. G., Mahadevan, L. & Lewis, J. A. Biomimetic 4D printing. *Nature Mater* **15**, 413–418 (2016).

24. Zou, B., Song, C., He, Z. & Ju, J. Encoding of direct 4D printing of isotropic single-material system for double-curvature and multimodal morphing. *Extreme Mechanics Letters* **54**, 101779 (2022).

25. Wang, L.-C. *et al.* Active Reconfigurable Tristable Square-Twist Origami. *Advanced Functional Materials* **30**, 1909087 (2020).

26. Boley, J. W. *et al.* Shape-shifting structured lattices via multimaterial 4D printing. *Proc. Natl. Acad. Sci. U.S.A.* **116**, 20856–20862 (2019).

27. Nojoomi, A., Jeon, J. & Yum, K. 2D material programming for 3D shaping. *Nat Commun* **12**, 603 (2021).

28. Kim, J., Hanna, J. A., Byun, M., Santangelo, C. D. & Hayward, R. C. Designing Responsive Buckled Surfaces by Halftone Gel Lithography. *Science* **335**, 1201–1205 (2012).

29. Sawhney, R. & Crane, K. Boundary First Flattening. *ACM Trans. Graph.* **37**, 1–14 (2018).

30. Nojoomi, A., Arslan, H., Lee, K. & Yum, K. Bioinspired 3D structures with programmable morphologies and motions. *Nat Commun* **9**, 3705 (2018).

31. Klein, Y., Efrati, E. & Sharon, E. Shaping of Elastic Sheets by Prescription of Non-Euclidean Metrics. *Science* **315**, 1116–1120 (2007).

32. Efrati, E., Sharon, E. & Kupferman, R. Elastic theory of unconstrained non-Euclidean plates. *Journal of the Mechanics and Physics of Solids* **57**, 762–775 (2009).

33. Siéfert, E., Levin, I. & Sharon, E. Euclidean Frustrated Ribbons. *Phys. Rev. X* **11**, 011062 (2021).

34. Tolley, M. T. *et al.* Self-folding origami: shape memory composites activated by uniform heating. *Smart Mater. Struct.* **23**, 094006 (2014).

35. Kotikian, A., Truby, R. L., Boley, J. W., White, T. J. & Lewis, J. A. 3D Printing of Liquid Crystal Elastomeric Actuators with Spatially Programed Nematic Order. *Advanced Materials* **30**, 1706164 (2018).

36. Yuk, H. & Zhao, X. A New 3D Printing Strategy by Harnessing Deformation, Instability, and Fracture of Viscoelastic Inks. *Advanced Materials* **30**, 1704028 (2018).

37. Kim, Y., Yuk, H., Zhao, R., Chester, S. A. & Zhao, X. Printing ferromagnetic domains for untethered fast-transforming soft materials. *Nature* **558**, 274–279 (2018).

38. Reddy, J. N. *Mechanics of Laminated Composite Plates and Shells: Theory and Analysis, Second Edition*. (CRC Press, 2003).

39. Yu, K., Ge, Q. & Qi, H. J. Reduced time as a unified parameter determining fixity and free recovery of shape memory polymers. *Nat Commun* **5**, 3066 (2014).

40. Van Manen, T., Janbaz, S. & Zadpoor, A. A. Programming 2D/3D shape-shifting with hobbyist 3D printers. *Mater. Horiz.* **4**, 1064–1069 (2017).

41. Yang, K., Xu, S., Shen, J., Zhou, S. & Xie, Y. M. Energy absorption of thin-walled tubes with pre-folded origami patterns: Numerical simulation and experimental verification. *Thin-Walled Structures* **103**, 33–44 (2016).

42. Lee, T.-U., You, Z. & Gattas, J. M. Elastica surface generation of curved-crease origami. *International Journal of Solids and Structures* **136–137**, 13–27 (2018).

43. Choi, G. P. T., Dudte, L. H. & Mahadevan, L. Programming shape using kirigami tessellations. *Nat. Mater.* **18**, 999–1004 (2019).

44. Bai, Y. *et al.* A dynamically reprogrammable surface with self-evolving shape morphing. *Nature* **609**, 701–708 (2022).

45. Gao, T., Bico, J. & Roman, B. Pneumatic cells toward absolute Gaussian morphing. (2023).

46. Treml, B., Gillman, A., Buskohl, P. & Vaia, R. Origami mechanologic. *Proc. Natl. Acad. Sci. U.S.A.* **115**, 6916–6921 (2018).

47. Cui, H. *et al.* Design and printing of proprioceptive three-dimensional architected robotic metamaterials. *Science* **376**, 1287–1293 (2022).

48. Dong, Y. *et al.* Untethered small-scale magnetic soft robot with programmable magnetization and integrated multifunctional modules. *Sci. Adv.* **8**, eabn8932 (2022).

49. Liu, K., Tachi, T. & Paulino, G. H. Invariant and smooth limit of discrete geometry folded from bistable origami leading to multistable metasurfaces. *Nat Commun* **10**, 4238 (2019).